metals

Article

Investigation of the Geometry of Metal Tube Walls after Necking in Uniaxial Tension

Chong Li, Daxin E *, Jingwen Zhang and Ning Yi

School of Materials Science and Engineering, Beijing Institute of Technology, Beijing 100081, China; lichong@bit.edu.cn (C.L.); mymoneyold@163.com (J.Z.); yi.ning@outlook.com (N.Y.)

* Correspondence: daxine@bit.edu.cn; Tel.: +86-136-6137-4667

Academic Editor: Enrique Louis
Received: 10 February 2017; Accepted: 14 March 2017; Published: 17 March 2017

Abstract: In order to characterize the deformation and true stress–strain relation of metal tubes, the geometry of tube walls after necking in uniaxial tension need to be determined. The paper investigated the necking process of metal tube. A large number of tensile tests and finite element analysis of 1Cr18Ni9Ti tubes with different sizes were conducted. It was found that the geometry of outer tube wall in the necking region can be described using a logistic regression model. The final geometry of the tube is determined by original tube diameter and wall thickness. The offset of tube walls are affected by two competing factors: volume constancy and necking. The offset distances of outer and inner walls are mainly affected by original wall thickness. The length of the necking zone is more influenced by original tube diameter. Tube elongation at fracture increases slightly as tube diameter gets larger, while the wall thickness has almost no impact on the elongation.

Keywords: tube tension; necking; surface profile; tube diameter; wall thickness

1. Introduction

Metal tubes have been widely used in many industrial applications because of their special characteristics including light weight, high strength, energy absorption [1], etc. There are increasing numbers of tubular parts in automobiles, ships and aircrafts that replace solid parts. Also in oil and gas fields, forming of pipelines is an extremely important issue. In the design stage of tube application, the prediction of tube forming failure is a key task. Finite element method is an indispensable tool to avoid many trial and error iterations [2]. The stress–strain relationship of the material is one of the most important input parameters to ensure the accuracy of finite element calculation, especially when plastic deformation occurs [3–5]. Due to the hollowed structure, the mechanical properties of metal tubes are different from the sheet metal [6] or round metal bars [7]. Tao and Yang described the tube sample's mechanical properties using the measurement of dog bone specimens which are cut from the tube samples [8]. However, the specimens after cut off may exhibit different mechanical behavior since the axial symmetry has been destroyed. Another assumption is that metal tubes share the same mechanical property as metal bars [9]. Apparently, these approximations are not accurate when analyzing the forming process of metal tubes [10]. Only the mechanical properties obtained from direct measurement from the tube specimens can characterize the forming mechanics of tube metals with a higher accuracy [11–15].

Rathnaweera et al. [16] studied the performance of aluminum tubes and Terocore® hybrid structures in quasi-static three-point bending. They observed that the bottom surface failure (tensile) from structures is one of the failure modes during bending and it occurred when the bottom surface of the outer tube reached the ultimate tensile strain. Finite element analysis (FEA) was carried out in a subsequent study by Hanssen et al. [17] using LS-DYNA (Livermore Software Technology Corporation, Livermore, CA, USA). However, a correlation between experimental results was not obtained, since they were unable to use a failure criterion in their model. They also pointed out that predicting failure by using damage mechanics on non-filled metal tubes is a complicated task in itself. Shi et al. [18] simulated the necking and fracture of tube under hydro forming. In the modeling approach, they determined the localized necking strain by examining the deformed configuration during tension and assumed the hoop strain was uniformly distributed in the circumferential direction. They claimed that the current model could not differentiate the deformations' development in the circumferential direction from the axial direction. Kofiani [19] proved that the necking simulation for tubes is very sensitive to the introduced material behavior and the element size.

In order to get more accurate simulated results for various tube forming processes, the more accurate stress–strain curve is the main difficulty at this stage. Moreover, the research focus on the most basic deformation of metal tubes, unaxial tension, is still far from complete. A standard uniaxial tensile test can achieve the true stress–strain curves up to the uniform elongation point. Once necking occurs, the conventional measurement methods such as using strain gauge are no longer valid due to the stress triaxiality [20]. Thus, using tensile test data directly as input into FEA will inevitably lead to prediction results bias.

Numerous studies were conducted to characterize the material's behavior after necking [20–30]. We could get some inspiration and reference from those of metal sheets and round bars. Wierzbicki et al. [22–26] developed a complete necking and fracture predictive technology for steel sheets. The inverse methods after necking for the simulation purposes were proposed. Bridgman's method is one of the widely accepted approaches, which generates analytical stress–strain relations by considering the geometry of the neck, such as curvature of the profile and diameter [27]. This method was further developed by other researches and has been applied to tensile specimens with both circular cross sections and rectangular cross sections [28–30]. Ling [28] calculated the true stress–strain functions from engineering stress–stain data of tensile strips by utilizing weighted averages of upper and lower bound of stress–strain curves. However, few literatures have reported applying this method in tubes. Apparently, the post-necking stress–strain relationships of tubes are crucial when designing the tube forming process such as hydro forming [31] or bending [32]. One of the difficulties when implementing Bridgman's method is the accurate measurement of necking profile. If a simple formula could be developed to describe the curvature profile of the neck, the derivation of the analytical model would extremely convenient.

In this study, an analytical formula was proposed to depict the curvature profile, which could easily be used in combination with Bridgman's equation in the future to derive the post-necking stress–strain relationships of tubes. The geometry of the neck—curvature profile and diameter—during uniaxial tension of tubes was investigated. Experiments and FEA were conducted to investigate the geometrical evolution of the neck and the smallest diameter of the neck just before or at fracture. Experiments, FEA and analytical formula exhibit excellent agreement on the curvature profile depiction. In addition, the neck diameter at fracture and elongation of different tube dimensions in uniaxial tension was also discussed, which is a good industrial reference for design analysis.

2. Materials and Methods

2.1. Material and Test Device

A conventional uniaxial tensile test was conducted first to obtain the stress–strain behavior of the tubes. Instead of cutting sections from tube wall, full cross-section tubes were tested directly to ensure the results can reflect the actual mechanical response of the specimen. A commonly used material 1Cr18N9Ti (C $\leq$ 0.12%, Si $\leq$ 1.0%, Mn $\leq$ 2.0%, P $\leq$ 0.035%, S $\leq$ 0.03%, Ti 0.50%–0.80%, Ni 8.00%–11.00%, Cr 17.00%–19.00%) was selected in this study. The tube size is defined by its outer diameter (OD) and inner diameter (ID) or wall thickness (WT). The tube sizes used in tensile test are listed in Table 1. At least 3 specimens were tested for each size.

Table 1. Sizes of 1Cr18Ni9Ti tube samples selected in experiment.

OD_0 WT_0	6 mm	8 mm	10 mm	12 mm	14 mm
0.6mm	○	×	×	×	×
1 mm	○	○	○	○	○
1.5 mm	○	○	×	×	×
2 mm	○	○	×	×	×
2.5 mm	○	×	×	×	×

WT_0 denotes the original tube wall thickness. OD_0 denotes the original outer tube diameter. "○" means the tube in this dimension is selected in experiment while "×" means not.

Tube specimens were cut based on the Standard GB/T 228-2002 [33]. In order to ensure the uniaxial tensile condition, two metal cylindrical plugs were inserted from the two open ends of each tube. The plugs were specially machined with a round top for easy operation. During tension, the grips clamped the two ends of the tube with plugs inserted. The dimension of tube samples and the plugs are shown in Figure 1a. Previous test experience shows that fracture may occasionally not occur in the middle of the tube. In order to ensure that the fracture occurs within the gauge length, two more pairs of marked lines (Gauge II and III) were drawn on the surface of each specimen besides the usual one in the middle part (Gauge I). Once the fracture occurs outside Gauge I, Gauge II or III could be selected for gauge length measurement according to the fracture location. WDW-E100 universal testing machine (Jinan Shijin Group Co. Ltd., Jinan, China) was used for the test, Figure 1b. Constant loading speed v = 2.5 mm/min was selected. Tension stopped once tube samples fractured. Strain level was recorded with an extensometer until 5% extension.

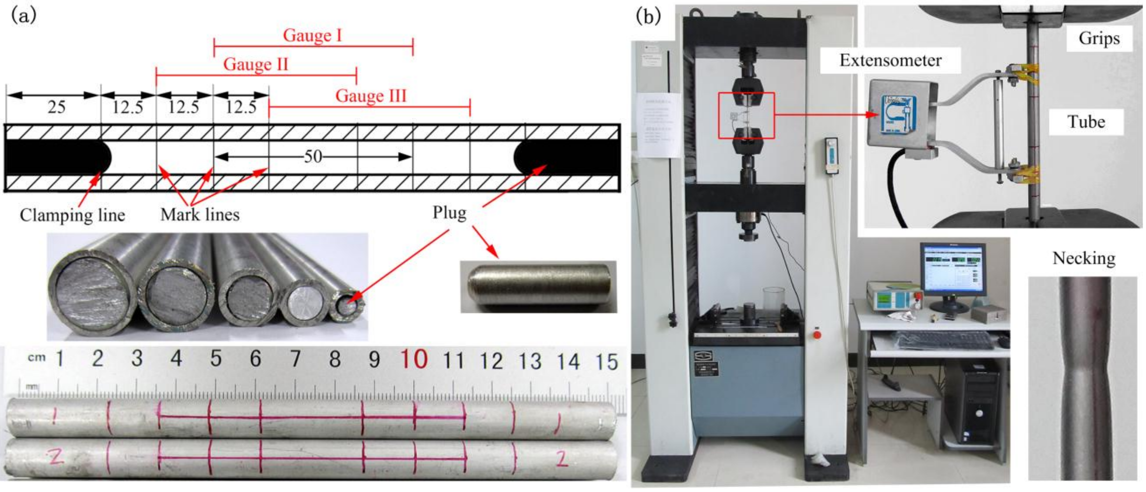

Figure 1. Specimens and test device: (**a**) dimension of the tube sample; (**b**) universal testing machine.

2.2. Mechanical Properties

Figure 2 shows the mechanical properties of tube 1Cr18Ni9Ti obtained from tensile test. From the engineering stress–strain curves in Figure 2a, it can be seen that tube samples with different sizes exhibit very similar mechanical response. For simplification, we picked the stress–strain curve of $OD_0 = 8$ mm and $WT_0 = 1$ to represent the mechanical response of all the tube specimens and to be used in finite element simulation as input. The effect of the deviation of stress–strain curves on the necking will be studied in future. Figure 2b shows true stress–strain relation before necking as calculated (solid line) and the extrapolated relation after necking (dotted line). The power law equation $\sigma = K\varepsilon^n$ was used to fit the material's stress–strain curve, where K is the strength coefficient and n is the strain hardening index. The mechanical properties coefficients are list in Figure 2b.

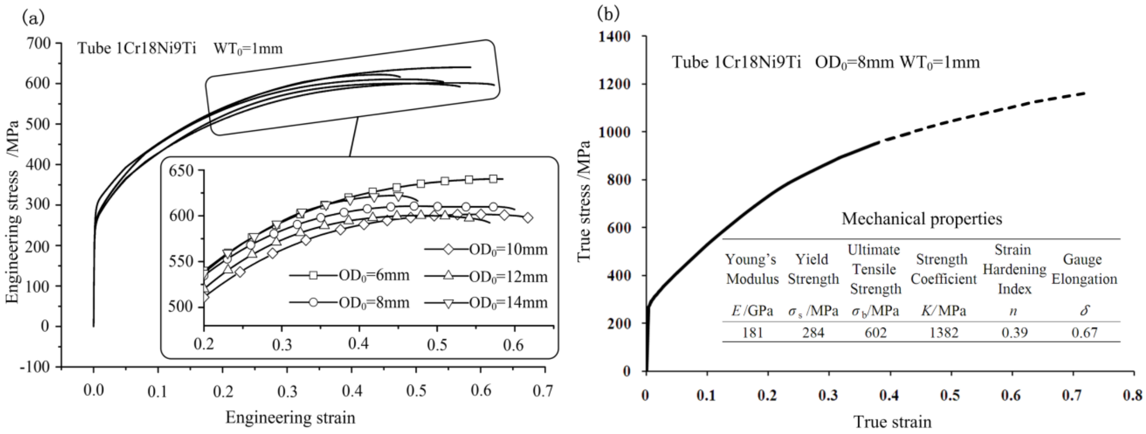

Young's Modulus	Yield Strength	Ultimate Tensile Strength	Strength Coefficient	Strain Hardening Index	Gauge Elongation
E/GPa	σ_s/MPa	σ_b/MPa	K/MPa	n	δ
181	284	602	1382	0.39	0.67

Figure 2. Material properties: (**a**) Engineering stress–strain curves of different sizes 1Cr18Ni9Ti tubes; (**b**) True stress–strain curve and mechanical properties of 1Cr18Ni9Ti with OD_0 = 8 mm WT_0 = 1.

2.3. Deformation Pattern of the Tube Walls

After tensile test, all the samples were cut along the axis of the tube. Figure 3 shows the shapes of the tube walls at fracture area with different outer diameters and wall thicknesses. It can be clearly seen that both inner diameter and outer diameter at necking region shrank after tube fracture. Here we define the original inner and outer diameters are ID_0 and OD_0 and the inner and outer diameters after fracture are ID_f and OD_f, respectively. Figure 3a shows that the shrinkage ratio of OD $((OD_0 - OD_f)/OD_0)$ increases as the original wall thickness WT_0 increases. The dimensional change of ID is slightly different. From the observation of Figure 3a,b, it can be found that the shrinkage ratio of ID $((ID_0 - ID_f)/ID_0)$ decreases as the thickness-diameter ratio WT_0/OD_0 increases. More details are discussed later.

(a) Unit: mm

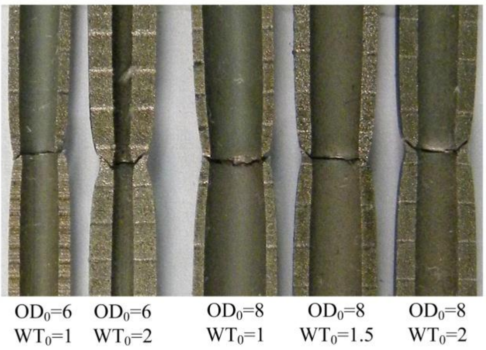

(b) WT$_0$=1 Unit: mm

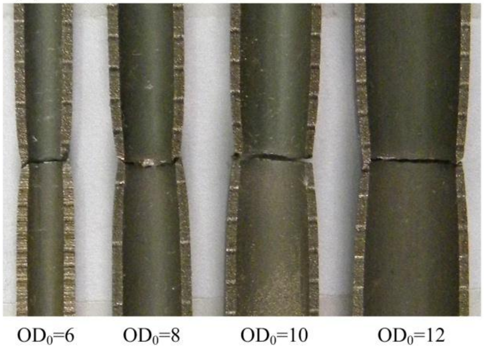

Figure 3. Geometries of tube walls at fracture area with (**a**) different wall thicknesses, and (**b**) different outer diameters.

2.4. Finite Element Model

Commercial finite element code Abaqus 6.10 (SIMULIA by Dassault Systèmes, Waltham, MA, USA) was used to model the uniaxial tension of tubes. Only a quarter tube with 12 mm length was modeled to save computation time, Figure 4. Three-dimensional hexahedral solid elements C3D8R were used in the model. Two-dimensional axial symmetric elements were not used in this study because the model will be used in future bending simulations, which are not axial symmetric forming processes. In order to accurately capture the stress–strain state during necking and fracture, a consistent finer element size (0.02 mm × 0.02 mm × 0.02 mm in necking zone) was used to mesh the critical area locally for all the tube sizes. The material's stress–strain curve and material properties in Figure 2b was used as FEA input. Although anisotropy can be caused by the rolling process of the tube, it is difficult to quantify the anisotropy coefficient. Thus, it is assumed in FEA modeling that the tube is isotropic. All six degrees of freedom were fixed at the bottom surface. A 2.5 mm/min velocity was set as the boundary condition at the top surface, which is the same as the loading condition in experiment. Symmetric boundary conditions were applied to enforce the axial symmetry.

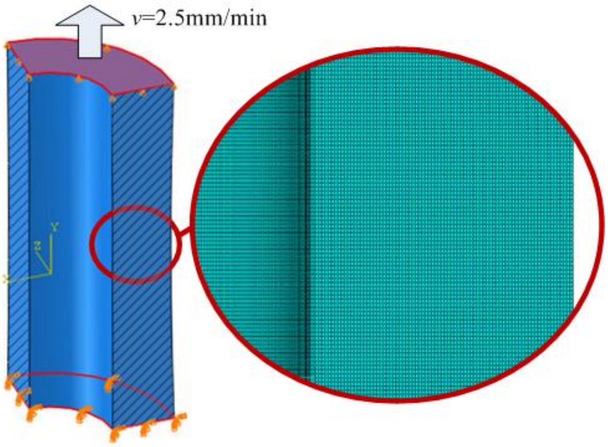

Figure 4. Finite element model of tube tension.

In order to trigger the necking process, a defect was put into the model manually at the middle of the tube (mesh refinement area), where OD_0 is 0.05 mm smaller than the nominal tube diameter. The simulation will stop once fracture is initiated so that the evolution of the tube's geometry during the necking process can be tracked. Thus, we still need to be able to identify the fracture initiation point even though fracture formation is not the focus of our study. In the FEA model, damage initiation, damage evolution and element removal embedded in ABAQUS solver were introduced to signal the ending point of the simulation.

Ductile criterion for damage initiation was utilized, as shown in Equation 1 [34].

$$\omega_D = \int \frac{d\bar{\varepsilon}^{pl}}{\bar{\varepsilon}_D^{pl}(\eta, \dot{\bar{\varepsilon}}^{pl})} = 1 \tag{1}$$

where ω_D is a state variable that increases monotonically with plastic deformation. The equivalent plastic strain at the onset of damage, $\bar{\varepsilon}^{pl}$, was a function of stress triaxiality η and strain rate $\dot{\bar{\varepsilon}}^{pl}$. $\bar{\varepsilon}^{pl}$ was equal to the strain hardening index $\bar{\varepsilon}^{pl} = n = 0.39$ [35], which was calculated from the material's stress–strain curve. The stress triaxiality for tensile test was 0.33. The damage evolution was defined based on plastic displacement $\bar{u}_D^{pl}$, which was defined with the evolution equation:

$$\dot{\bar{u}}^{pl} = L\dot{\bar{\varepsilon}}^{pl} \tag{2}$$

where L is the characteristic length of the element. Assuming a linear evolution of the damage variable with effective plastic displacement and the effective plastic displacement at failure, $\overline{\mathrm{u}}_{\mathrm{f}}^{\mathrm{pl}} = 0.035$ was calibrated using the test data of tube with OD_0 = 8 mm and WT_0 = 1. Then the damage variable increases according to Equation (3). The maximum degradation was set.

$$\dot{d} = \frac{L\dot{\bar{\varepsilon}}^{pl}}{\bar{u}_f^{pl}} = \frac{\dot{\bar{u}}^{pl}}{\bar{u}_f^{pl}} \tag{3}$$

To ensure $\bar{u}_f^{pl} = 0.035$ was applicable in tubes with different sizes, the element sizes were kept uniform in all FEA models.

3. Results and Discussion

In order to compare the results with ease, we have to pick a suitable coordinate system. In this study, the origin O of the coordinate is selected at the center point of the straight line which coincides with the tube wall of the straight tube section. $X = 0$ corresponds to the minimum OD_f location after necking and fracture. Positive y direction points opposite to the tube axis. Due to the fact that the tube deformation is almost symmetric about the y-axis, only the offset distance values in the $x > 0$ domain were extracted and the entire curves were mirrored about the y-axis when needed.

3.1. Logistic Regression Model and Validation of Finite Element Analysis (FEA) Calculation

It is found that the outer wall profile in the necking region can be described using a logistic regression model, as shown in Figure 5. The red dotted line in Figure 5a is the center line of the necked tube. The shapes of the tube on both sides of the center line are symmetrical. Red lines shows the profile of the necked tube in both FEA and tensile test (Figure 5a) have the same trend with the logistic regression model (Figure 5b). Logistic regression was developed by statistician David Cox in 1958 [36,37]. The logistic function is shown below.

$$y = \frac{A_1 - A_2}{1 + (x/x_0)^p} + A_2 \tag{4}$$

where A_1 is the lower boundary of the curve and A_2 is the upper boundary of the curve. x_0 is at the center of curvature. p denotes the slope of the curve.

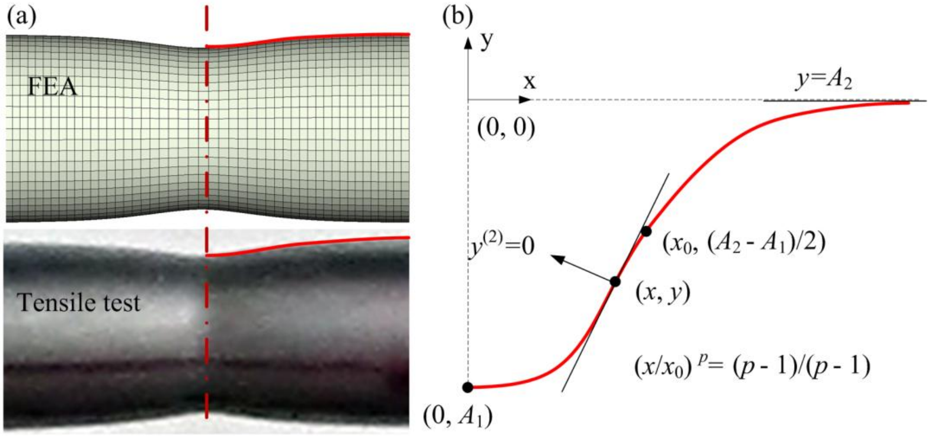

Figure 5. Schematic diagram of logistic regression model: (**a**) a curve that describes the profile of outer wall; (**b**) mathematical model of logistic regression.

If we select the offset distance in the y direction of outer tube wall outside the necking zone (straight section of the tube) as zero, then $A_2 = 0$. The model can be simplified as follow.

$$y = \frac{A}{1 + (x/x_0)^p} \tag{5}$$

where A denotes the maximum (in absolute value) offset distance of the outer wall.

Using the logistic regression, we can fit the parameters of A, x_0 and p with test data. Tables 2 and 3 show the fitted parameters of the logistic regression model for different tube sizes at fracture moment in tension test. The curves drawn using this model can be assumed as the actual outer wall profile of the tubes after necking. Thus, we can easily obtain the entire tube surface profile and the offset distance by the logistic regression model with only a few data points.

Finite element model can also predict the outer wall profile in the necking zone. Finite element simulations were conducted for the tube model OD_0 = 6 mm with different wall thickness and WT_0 = 1 mm with different OD_0 values. The outer wall profiles at fracture were extracted from the results and put together with the test data and logistic fitted curves in Figures 6 and 7.

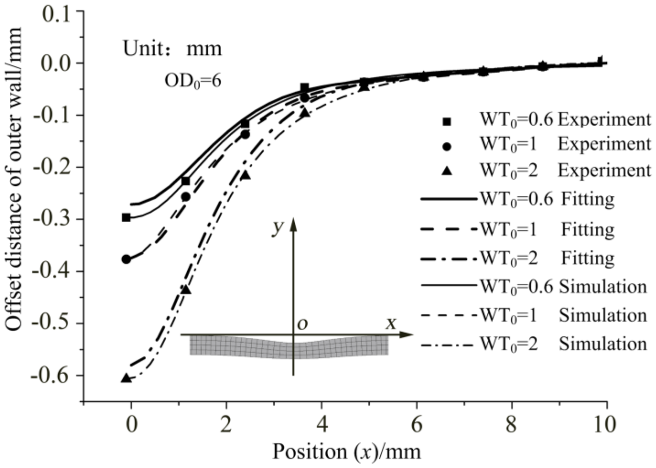

Figure 6. Outer wall profiles at fracture from tensile test and simulation and the logistic regression fitted curves in different wall thicknesses.

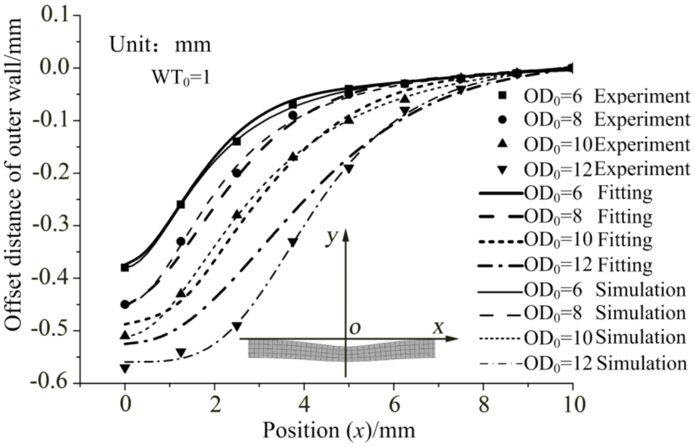

Figure 7. Inner wall profiles at fracture from tensile test and simulation results and the logistic regression fitted curves in different outer diameters.

The comparison shows that the outer wall profile calculated from finite element analysis (FEA) correlates with the test data and logistic model very well. The maximum error on Figure 6 is less than 0.03 mm (when WT_0 = 2 mm), while the maximum error on Figure 7 is smaller than 0.1 mm (when OD_0 = 12 mm). The excellent agreement between FEA and test data indicates that the finite element model used in this study can predict the tube deformation with great accuracy, and that we can rely on the FEA results to study tube forming mechanics in detail.

Table 2. Fitted parameters of the logistic regression model for OD_0 = 6mm tubes with different WT_0.

Wall Thickness (mm)	Max Offset Distance of Outer Wall (mm)	*A* (mm)	x_0 (mm)	*p*
$WT_0 = 0.6$	−0.3	−0.3	1.96	2.11
$WT_0 = 1$	−0.38	−0.38	1.93	2.01
$WT_0 = 2$	−0.61	−0.61	1.95	2.24

Table 3. Fitted parameters of the Logistic regression model for WT_0 = 1 mm tubes with different OD_0.

Outer Diameter (mm)	Max Offset Distance of Outer Wall (mm)	*A* (mm)	x_0 (mm)	*p*
$OD_0 = 6$	−0.38	−0.38	1.93	2.01
$OD_0 = 8$	−0.45	−0.45	2.22	2.02
$OD_0 = 10$	−0.51	−0.51	3.00	2.08
$OD_0 = 12$	−0.57	−0.57	4.26	3.43

3.2. Surface Profile Evolution of Inner and Outer Wall

The effect of original tube wall thickness on surface profile at fracture moment is displayed in Figure 8. Figure 8a shows that when OD_0 = 6 mm, the minimum diameter of outer wall at necking zone is inversely proportional to the wall thickness. In other words, necking is more prominent if the original tube wall is thicker. The length of the necking zone increases very slightly when the wall becomes thicker.

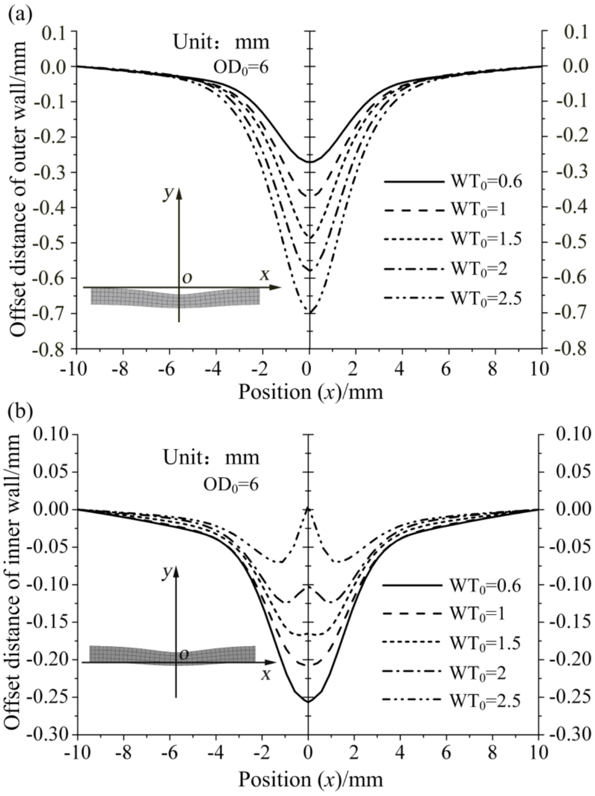

Figure 8. Effect of WT_0 on surface profile at fracture of (**a**) outer wall and (**b**) inner wall.

The surface profile of inner wall at fracture moment in Figure 8b shows an opposite trend. The shrinkage of ID decreases as wall thickness increases. When WT_0 = 1.5 mm, the maximum offset (the minimum ID) appears at $x = \pm 0.5$ instead of $x = 0$. As WT_0 increases beyond two millimeters, the inner wall offsets negatively first and then changes direction. As a result, the final inner wall profile shows a "W" shape. When $WT_0 = 2.5$ mm, the later expansion of ID at $x = 0$ is so dominant and the final ID_f value here is already greater than that in the straight section of the tube (the tube outside the necking region). The expansion is about 0.05 mm.

This phenomenon can be explained by the competing effects of volume constancy and necking. During tension, the tube becomes longer and both OD and ID should become smaller due to the fact of volume constancy. Once necking occurs, the wall of the tube tends to get thinner rapidly. Wall thinning means OD becomes smaller while ID becomes larger and both of them move toward the "mid-layer" of the wall thickness. Both volume constancy and necking tend to make OD become smaller. As a result, the overall shrinkage of OD is the superposition of these two effects. While for ID, the volume constancy tends to make ID become smaller. However, the necking effect will cause the ID become larger. In other words, the two effects are making ID moving in opposite directions. The inner wall profile (or ID_f) is determined by the dominancy of these two factors. When the original wall thickness is small (here $WT_0 < 1.5$ mm), the necking effect is not significant. Therefore, ID is still shrinking, yet the rate is still slower than OD. Once the original wall thickness is large enough (here $WT_0 > 2$ mm), the necking effect is dominant and the expansion rate is larger than the shrinking rate. Therefore, the superposition of the two factors will result in the expansion of ID.

Figure 9 shows the effect of OD_0 on the tube's surface profile. It indicates the offset distances of both outer and inner walls reach maximum at $x = 0$ (both OD_f and ID_f reach the minimum values). The offset distances of both outer and inner walls increase as OD_0 increases. Also, the rate of increase slows down as OD_0 becomes larger. When OD_0 increases from 10 to 12 mm, the shrinkage of OD_f is 0.038 mm, while the shrinkage of ID_f is only 0.014 mm. This means the offset distances of the inner wall becomes less affected as the tube OD_0 becomes larger and larger.

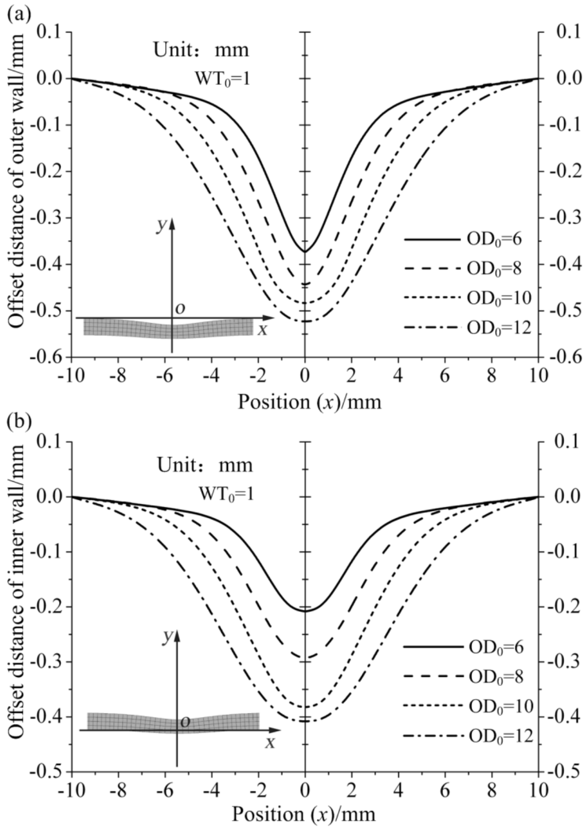

Figure 9. Effect of OD_0 on surface profile at fracture of (**a**) the outer wall and (**b**) the inner wall.

From results in Figures 8 and 9, it can be found that WT_0 has stronger influence on the offset distance, while OD_0 has a greater influence on the necking length.

3.3. The Inner Surface Profile Change during Necking

From both experiment and simulation, it can be observed that OD of the tube keeps decreasing as tension continues, while the geometrical change of the inner tube wall is more complicated. Previous discussion indicates that the offset of the inner tube wall is the consequence of two competing factors: volume constancy and necking. A detailed finite element analysis of inner wall profile evolution during necking in the tensile test is presented next.

Figure 10 shows the finite element results of the profile of inner wall at five different time steps during tension of a tube with OD_0 = 6 mm, WT_0 = 2 mm. The time steps are selected at same intervals from the beginning of necking till fracture. It can be seen that at the beginning stage of necking (step 1 to step 2), the whole inner wall surface offsets negatively (toward the axis of the tube). This indicates the necking effect is not obvious at this time. From step 3, the inner wall close to $x = 0$ starts to move backwards, while the wall surface area around $x = 1$ continues to move negatively. Starting from this time step, the necking effect becomes dominant and the speed of wall thinning is much faster than the reduction of diameter. The different direction of motion at center ($-1 < x < 1$) and other areas ($x > 1$ and $x < -1$) indicates the necking is a highly local effect that only changes the material's deformation at a very small area. This explains the formation of the "W" shape at the inner wall surface. Steps 4 and 5 show that the necking effect grows extremely quickly and the inner wall surface close to $x = 0$ offsets outwards rapidly in positive direction. The offset distance at $x = 0$ becomes even larger than zero. This is because necking is a fairly local effect and very little material is involved in this deformation. After step 5, the wall thickness at $x = 0$ will decrease rapidly till fracture.

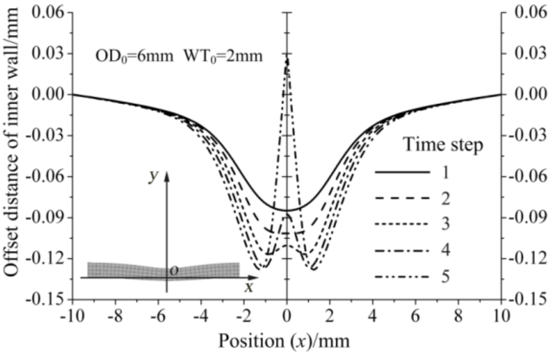

Figure 10. Geometrical change of inner tube wall during necking process.

Figure 11 shows an equivalent plastic strain contour in the quarter model of a tube with OD_0 = 8 mm and WT_0 = 2 mm. At the beginning of necking (Status 1 and 2), the inner wall moves inwards. At Status 1, the strain in the wall of the tube is still uniformly distributed in the middle section of the tube. From Status 2, higher strain starts to concentrate at a small local area, which indicates the necking effect is becoming obvious. At Status 3, the necking effect is very significant and two necking bands have formed. High strain concentration is shown within the necking bands. A local area on the inner wall surface where two necking bands intersect starts to move outwards. Status 3 is a special moment when the offset distance of the inner wall in the middle of the necking zone is equal to that at the straight section of the tube. At Status 4, the ID at the same location grows larger and ultimately causes fracture.

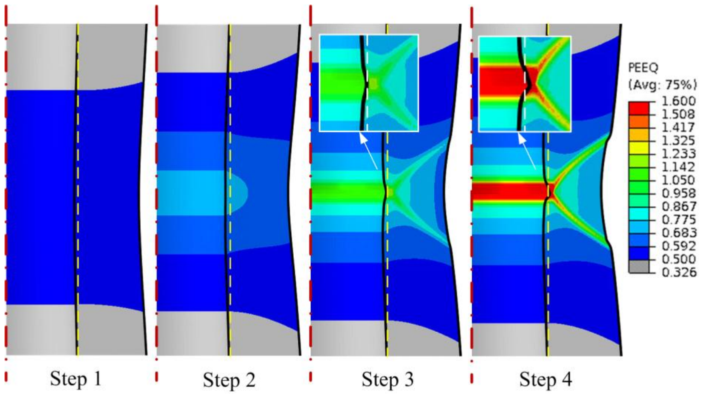

Figure 11. Offset status change of the inner wall in a tube with OD_0 = 8mm and WT_0 = 2mm.

3.4. Effect of Original Diameter and Wall Thickness on the Diameter and Elongation at Fracture

Figure 12 shows the influence of OD_0 and WT_0 on the diameter of the neck at fracture, OD_f. The data from FEA are the smallest outer diameter of the tube when the fracture just begins. Since it is difficult to judge when the fracture will begin and stop the tension without delay during the experiment, OD_f from tensile tests are measured after fracture. The FEA results are in good agreement with the experimental data. Figure 12a,b shows that when WT_0 remains constant, OD_f increases linearly with increasing OD_0. When OD_0 remains constant, OD_f decreases linearly as WT_0 increases. In Figure 12c, the tube diameter shrinkage ratio at fracture is defined as $(OD_0 - OD_f)/OD_0$. It can be observed that when WT_0 remains constant, the shrinkage ratio of outer diameter at fracture changes very little and generally maintains at around 0.31. And in Figure 12d, when OD_0 remains constant, the shrinkage ratio increases linearly with WT_0. This is why OD_f is linearly proportional to OD_0 and is inversely linearly proportional to WT_0.

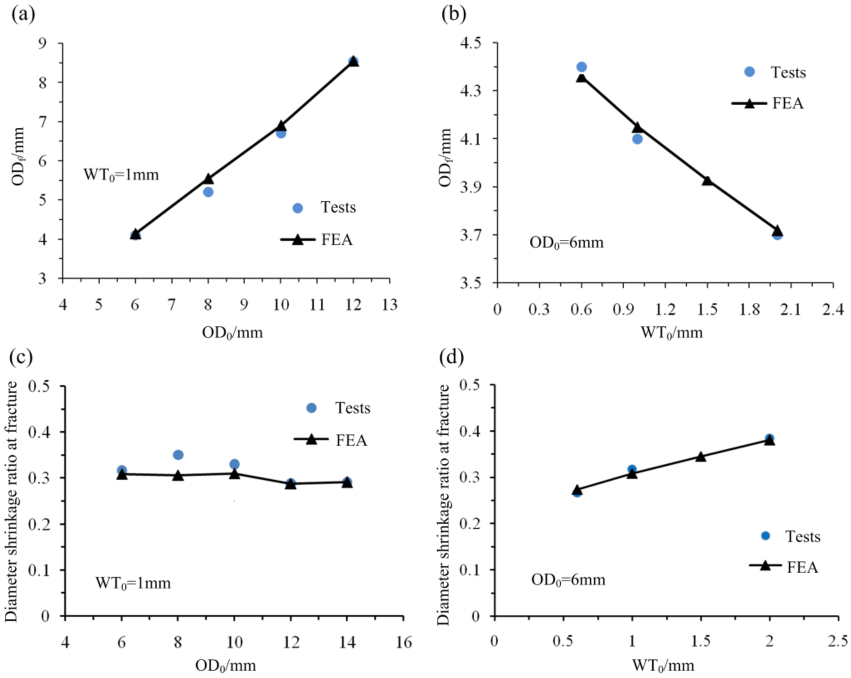

Figure 12. Effect of original diameter and wall thickness on tube diameter at fracture: (**a**) Effect of original diameter on fracture diameter; (**b**) Effect of original wall thickness on fracture diameter; (**c**) Effect of original diameter on diameter shrinkage; (**d**) Effect of original wall thickness on diameter shrinkage.

In the same way as above, the elongation at fracture of the gauge section calculated from experiment and finite element simulation, respectively, are plotted in the Figure 13. It reveals the effect of OD_0 and WT_0 on tube elongation at fracture. The data from tensile tests are always a little bit larger than those from FEA; one of the reasons should come from the measure moment. We get the gauge elongation at fracture once the fracture begins in FEA but after fracture in tensile tests. The average error is about five percent, but the curves have the same trend. In Figure 13a, as OD_0 gets larger, tube elongation increases slightly. In Figure 13b, as WT_0 getting larger, tube elongation almost keeps the same value. The elongation becomes more affected by OD_0 and less affected by changes in WT_0. It can be inferred that the wall thickness has almost no impact on the elongation at fracture in a small-diameter thin-walled 1Cr18Ni9Ti tube.

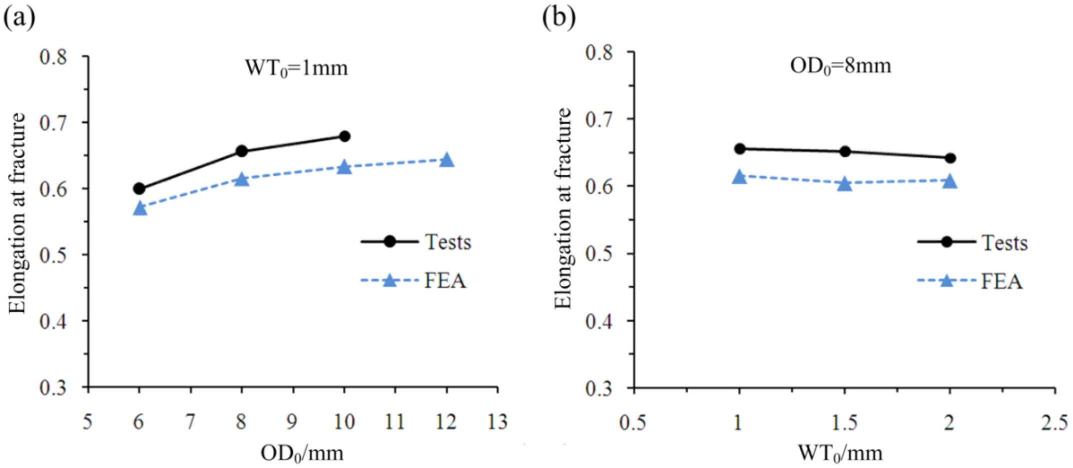

Figure 13. Effect of (**a**) original diameter and (**b**) original wall thickness on the elongation at fracture.

4. Conclusions

A large number of tensile tests of 1Cr18Ni9Ti tubes with different sizes were conducted. Finite element method demonstrated its advantages in studying the tube forming mechanics. Surface profiles of the tube walls from finite element simulation can match the test data with high accuracy. Combined with a large number of experiments and FEA results, the following conclusions can be made.

(1) The geometry of outer tube wall in the necking region can be described using a logistic regression curve. Thus, the mathematical formula of necked tube surface profile and the offset distance can be obtained by the calculated logistic regression model with only a few data points. The formula could be used in combination with Bridgman's equation in the future to derive the post-necking stress–strain relationships of tubes.

(2) During the uniaxial tension of tube, both OD and ID have a shrinking trend, though the shrinking rates are different. The offset distance of outer tube wall increases as the original wall thickness or outer tube diameter increases. The offset distance of inner tube wall decreases as the original wall thickness increases. If the wall of the tube is thick enough, the final inner wall will expand instead of shrinking.

(3) The offset (shrinking or expansion) of OD and ID are affected by two competing factors: volume constancy and necking. For the case of OD, both factors will cause the OD shrink. So OD shrinks faster when necking becomes dominant. However, for the case of ID, the two factors will cause the ID to move in opposite directions. The final motion of the ID is determined by the dominant factor.

(4) The final geometry of the tube is determined by the original outer tube diameter and wall thickness. The offset distances of outer and inner walls are mainly affected by the original wall thickness. The length of the necking zone is more influenced by the original outer tube diameter.

(5) Tube outer diameter at fracture moment is linearly proportional to original diameter and is inversely linearly proportional to original wall thickness. Because when original wall thickness remains constant, the outer diameter shrinkage ratio at fracture remains almost unchanged and when original diameter remains constant, the shrinkage ratio increases linearly with original wall thickness. As tube diameter getting larger, the tube elongation increases slightly. The wall thickness has almost no impact on the elongation at fracture in small-diameter thin-walled 1Cr18Ni9Ti tube.

Acknowledgments: The work described in the paper was part of research within the program Grant No. 51175044 from National Natural Science Foundation of China under. The authors are very grateful for the financial support.

Author Contributions: Chong Li and Jingwen Zhang conceived and designed the experiments; Chong Li, Ning Yi and Jingwen Zhang performed the experiments. Chong Li performed the finite element simulations, analyzed the date and wrote the manuscript. Daxin E supervised the whole study. All authors reviewed the final paper.

Conflicts of Interest: The authors declare no conflict of interest.

References

1. Alghamdi, A.A.A. Collapsible impact energy absorbers: An overview. *Thin-Walled Struct.* **2001**, *39*, 189–213. [CrossRef]
2. Kim, J.H.; Serpantié, A.; Barlat, F.; Pierron, F.; Lee, M.G. Characterization of the post-necking strain hardening behavior using the virtual fields method. *Int. J. Solids Struct.* **2013**, *50*, 3829–3842. [CrossRef]
3. Liu, Z.; Ji, F.; Zhu, T. One-Dimensional Constitutive Model for Porous Titanium Alloy at Various Strain Rates and Temperatures. *Metals* **2017**, *7*, 24. [CrossRef]
4. Yang, L.C.; Pan, Y.T.; Chen, I.G.; Lin, D.Y. Constitutive relationship modeling and characterization of flow behavior under hot working for Fe–Cr–Ni–W–Cu–Co super-austenitic stainless steel. *Metals* **2015**, *5*, 1717–1731. [CrossRef]
5. Lin, F.; Dong, Y.; Kuang, X.; Lu, L. Strain Rate Behavior in Tension of Reinforcing Steels HPB235, HRB335, HRB400, and HRB500. *Materials* **2016**, *9*, 1013. [CrossRef]
6. Li, C.; Daxin, E.; Ning, Y. Analysis on fracture initiation and fracture angle in ductile sheet metal under uniaxial tension by experiments and finite element simulations. *J. Mater. Res.* **2016**, *31*, 3991–3999. [CrossRef]
7. Tvergaard, V.; Needleman, A. Analysis of the cup-cone fracture in a round tensile bar. *Acta Metall.* **1984**, *32*, 157–169. [CrossRef]
8. Tao, Z.; Yang, H.; Li, H.; Fan, X. Quasi-static tensile behavior of large-diameter thin-walled Ti–6Al–4V tubes at elevated temperature. *Chin. J. Aeronaut.* **2016**, *29*, 542–553. [CrossRef]
9. Mattos, H.S.C.; Chimisso, F.E.G. Necking of elasto-plastic rods under tension. *Int. J. Nonlinear Mech.* **1997**, *32*, 1077–1086. [CrossRef]
10. Pepelnjak, T.; Šašek, P.; Kudlaček, J. Upsetting Analysis of High-Strength Tubular Specimens with the Taguchi Method. *Metals* **2016**, *6*, 257. [CrossRef]
11. Sokolowski, T.; Gerke, K.; Ahmetoglu, M.; Altan, T. Evaluation of tube formability and material characteristics: Hydraulic bulge testing of tubes. *J. Mater. Process. Technol.* **2000**, *98*, 34–40. [CrossRef]
12. He, Z.; Lin, Y.; Wu, J.; Yuan, S. Study on the Formability and Deformation Behavior of AZ31B Tube at Elevated Temperature by Tube Bulging Test. *J. Mater. Eng. Perform.* **2011**, *20*, 1278–1284. [CrossRef]
13. Jeong, H.S.; Jeon, J.W.; Ha, M.Y.; Cho, J.R. Finite element analysis for inconel 625 fine tube bending to predict deformation characteristics. *Int. J. Precis. Eng. Manuf.* **2012**, *13*, 1395–1401. [CrossRef]
14. Daxin, E.; Liu, Y. Springback and time-dependent springback of 1Cr18Ni9Ti stainless steel tubes under bending. *Mater. Des.* **2010**, *31*, 1256–1261. [CrossRef]
15. Ghazijahani, T.G.; Jiao, H.; Holloway, D. Experiments on Dented Steel Tubes under Bending. *Adv. Struct. Eng.* **2015**, *18*, 1807–1818. [CrossRef]

16. Rathnaweera, G.; Dong, R.; Hajj, M.; Durandet, Y. Performance of aluminium/Terocore® hybrid structures in quasi-static three-point bending: Experimental and finite element analysis study. *Mater. Des.* **2014**, *54*, 880–892. [CrossRef]
17. Hanssen, A.G.; Hopperstad, O.S.; Langseth, M.; Ilatad, H. Validation of constitutive models applicable to aluminium foams. *Int. J. Mech. Sci.* **2002**, *44*, 359–406. [CrossRef]
18. Shi, Y.; Jin, H.; Wu, P.D.; Lloyd, D.J. Effects of superimposed hydrostatic pressure on necking and fracture of tube under hydroforming. *Int. J. Solids Struct.* **2017**. [CrossRef]
19. Kofiani, K.N. *Ductile Fracture and Structural Integrity of Pipelines & Risers*; Massachusetts Institute of Technology: Cambridge, MA, USA, 2013.
20. Mirone, G. A new model for the elastoplastic characterization and the stress–strain determination on the necking section of a tensile specimen. *Int. J. Solids Struct.* **2004**, *41*, 3545–3564. [CrossRef]
21. Bettaieb, M.B.; Abed-Meraim, F. Effect of kinematic hardening on localized necking in substrate-supported metal layers. *Int. J. Mech. Sci.* **2017**, *123*, 177–197. [CrossRef]
22. Wierzbicki, T.; Bao, Y.; Lee, Y.W.; Bai, Y. Calibration and evaluation of seven fracture models. *Int. J. Mech. Sci.* **2005**, *47*, 719–743. [CrossRef]
23. Lee, Y.W.; Woertz, J.C.; Wierzbicki, T. Fracture prediction of thin plates under hemi-spherical punch with calibration and experimental verification. *Int. J. Mech. Sci.* **2004**, *46*, 751–781. [CrossRef]
24. Bai, Y.; Wierzbicki, T. A new model of metal plasticity and fracture with pressure and Lode dependence. *Int. J. Plast.* **2008**, *24*, 1071–1096. [CrossRef]
25. Xue, L.; Wierzbicki, T. Numerical simulation of fracture mode transition in ductile plates. *Int. J. Solids Struct.* **2009**, *46*, 1423–1435. [CrossRef]
26. Li, Y.; Luo, M.; Gerlach, J.; Wierzbicki, T. Prediction of shear-induced fracture in sheet metal forming. *J. Mater. Process. Technol.* **2010**, *210*, 1858–1869. [CrossRef]
27. Bridgman, P.W. *Studies in Large Plastic Flow and Fracture*; McGraw-Hill: New York, NY, USA, 1952.
28. Ling, Y. Uniaxial True Stress-Strain after Necking. *AMP J. Technol.* **1996**, *5*, 37–48.
29. Zhang, Z.; Hauge, M.; Ødegård, J.; Thaulow, C. Determining material true stress–strain curve from tensile specimens with rectangular cross-section. *Int. J. Solids Struct.* **1999**, *36*, 3497–3516. [CrossRef]
30. Cabezas, E.E.; Celentano, D.J. Experimental and numerical analysis of the tensile test using sheet specimens. *Finite Elem. Anal. Des.* **2004**, *40*, 555–575. [CrossRef]
31. Wang, X.; Li, P.; Wang, R. Study on hydro-forming technology of manufacturing bimetallic CRA-lined pipe. *Int. J. Mach. Tools Manuf.* **2005**, *45*, 373–378. [CrossRef]
32. Limam, A.; Lee, L.H.; Corona, E.; Kyriakides, S. Inelastic wrinkling and collapse of tubes under combined bending and internal pressure. *Int. J. Mech. Sci.* **2010**, *52*, 637–647. [CrossRef]
33. Standard GB/T 228–2002. *Metallic materials—Tensile Testing at Ambient Temperature*; Standard Press of China: Beijing, China, 2002.
34. *Abaqus Analysis User's Manual, Version 6.10*; Dassault Simulia Company: Providence, RI, USA, 2010. Available online: http://abaqusdoc.ucalgary.ca/books/usb/default.htm (accessed on 15 March 2017).
35. Hill, R. On discontinuous plastic states, with special reference to localized necking in thin sheets. *J. Mech. Phys. Solids* **1952**, *1*, 19–30. [CrossRef]
36. Walker, S.H.; Duncan, D.B. Estimation of the probability of an event as a function of several independent variables. *Biometrika* **1967**, *54*, 167–179. [CrossRef] [PubMed]
37. Cox, D.R. The regression analysis of binary sequences. *J. R. Stat. Soc.* **1958**, *20*, 215–242.